Analysis of Ligand Binding and Protein Dynamics of Human Retinoid X Receptor Alpha Ligand-Binding Domain by Nuclear Magnetic Resonance†

Jianyun Lu,‡ David P. Cistola,§ and Ellen Li*,‡,§

Departments of Internal Medicine and Biochemistry and Molecular Biophysics, Washington University School of Medicine, St. Louis, Missouri 63110

Received July 26, 2005; Revised Manuscript Received November 17, 2005

ABSTRACT: Retinoid X receptors (RXRs) are nuclear receptors that can activate transcription as homodimers or as obligate heterodimeric partners of other nuclear receptors. While the crystal structures of the RXR ligand-binding domains (LBD) have been previously determined, the dynamics of activation is less well characterized at an atomic level. To probe the effect of ligand binding on RXR LBD dynamics, we initiated nuclear magnetic resonance studies of recombinant human RXRα LBD (T223−T462) with and without bound 9-*cis*-retinoic acid (9cRA). The ^{1}HN, ^{15}N, ^{13}Cα, ^{13}CO, and ^{13}C$^{\beta}$ resonance assignments were established for 164 of 240 residues in apo-RXRα LBD. Resonances corresponding to an additional 47 residues emerged upon 9cRA binding. These additional residues included those located in the vicinity of the ligand-binding pocket (helices H3, H5, and strands S1, S2), as well as residues located at the dimerization interface (helices H9 and H10). Thus 9cRA binding stabilized the ligand-binding pocket and had allosteric effects on the dimerization interface. Ligand-induced chemical shift perturbations outside the binding cavity were mapped to helix H3 and the AF-2 helix H12, indicating conformational changes in these regions. However, helix H11, a component of the tetramerization interface, and a large part of helix H10, a component of the dimerization interface, remained undetectable even after 9cRA binding. Although apo- and holo-hRXRα LBD existed predominantly as homodimers in solution, exchange between monomeric, dimeric, and tetrameric forms of the protein could have contributed to line broadening of cross-peaks corresponding to helices H10 and H11. ^{15}N T_1, T_2, and steady-state {^{1}H}−^{15}N NOE data collected at 500 and 700 MHz static magnetic fields showed that the internal motions for the residues in the H1−H3 loop (K245−D263) were much less restricted than those in the protein core for both apo- and holo-forms. Significant exchange R_{ex} contributions to the transverse relaxation rate were detected for most of the residues measured in both apo- and holo-RXRα LBDs by transverse relaxation optimized spectroscopy−Carr−Purcell−Meiboom−Gill (CPMG) experiments at two B_1 field strengths. Taken together these results suggest that the RXRα LBD exists as a dynamic ensemble of conformations, even after binding its cognate ligand. Such dynamic characteristics may allow RXRα to partner with multiple nuclear receptors.

Retinoid X receptors (RXR α, β, γ)[1] belong to the nuclear receptor (NR) superfamily of ligand-dependent transcription factors (*1*). They bind to DNA response elements as homodimers and homotetramers or as obligate heterodimer partners with a large number of other nuclear receptors, such as the peroxisome proliferator-activated receptors (PPARs), liver oxysterol receptors (LXRs), retinoic acid receptors (RARs), vitamin D receptor (VDR), and thyroid hormone receptors (TRs). In addition to its transcriptional activities, RXR can also regulate the nuclear import and export of their heterodimeric partners, such as Nur77/thyroid hormone receptor 3 (TR3), and play an important role in Nur77-dependent apoptosis (*2*). Two RXR agonists, 9-*cis*-retinoic acid (9cRA) and bexarotene, are currently used for the treatment of cancer and may prove useful for chemoprevention (*3*−*5*). There is evidence that synthetic RXR antagonists may be clinically useful in the treatment of obesity and related diseases such as type-2 diabetes (*6*). Thus the RXRs serve as master regulators of multiple nuclear hormone and lipid-signaling pathways and have emerged as important drug targets.

RXRs share the structural organization of NR superfamily consisting of an N-terminal ligand independent activation

† This work was supported by grants from the National Institutes of Health (NIH) DK59501 (E.L.), Washington University Digestive Diseases Research Core Center (DK 52574)−Protein Structure and Macromolecular Graphics Core, a pilot/feasibility award (J.L.) from the Washington University Center for Human Nutrition (DK56341). Spectra were collected at Washington University Molecular Biophysics NMR laboratory and High-Resolution NMR Service Facility in Chemistry, which is funded in part by the NIH through NCRR shared Instrument Grant RR015715.

* To whom correspondence should be addressed. Washington University School of Medicine, 660 South Euclid Ave., Campus Box 8124, St. Louis, MO 63110 Phone: 1−314-362-1072. Fax: 1−314-362-2312. E-mail: Eli@wustl.edu.

‡ Department of Internal Medicine.

§ Department of Biochemistry and Molecular Biophysics.

[1] Abbreviations: RXR, retinoid X receptor; NR, nuclear receptor; DNA, deoxyribonucleic acid; DBD, DNA binding domain; LBD, ligand-binding domain; PPAR, peroxisome proliferator-activated receptors; LXR, liver oxysterol receptors; RARs, retinoic acid receptors; VDR, vitamin D receptors; TR, thyroid homrone receptors; TR3, Nurr77/thyroid horomone receptor 3; 9cRA, 9-*cis*-retinoic acid; NMR, nuclear magnetic resonance; TROSY, transverse relaxation-optimized spectroscopy; IPTG, isopropyl-β-D-thiogalactopyranoside; β-ME, β-mercaptoethanol; DSS, dimethylsilapentane-5-sulfonic acid; CPMG, Carr−Purcell−Meiboom−Gill.

10.1021/bi051474j CCC: $33.50
Published on Web 01/24/2006

domain or the AB domain, a conserved DNA binding domain (DBD), a flexible hinge region, and a C-terminal ligand-binding domain (LBD), which also contains the dimerization interface and the ligand-dependent activation function AF-2 (*1*). The purified RXR ligand-binding domain exists as monomers, dimers, or tetramers in solution (*7*−*9*). A comparison of the crystallographic structure of the apo-RXRα LBD homodimer (*10*) and 9cRA bound monomer (*11*) reveals the largest structural rearrangements in helix H11, the H11−H12 loop and helix H12. In the apo-RXRα LBD homodimer, helix H12 protrudes out from the protein core. In the holo-RXRα LBD monomer, helix H12 is folded back against the ligand-binding pocket. Binding of 9cRA also induces a significant realignment of helix H3. The H1−H3 connecting region forms a helix, H2, in the apo-RXRα LBD crystal structure (*10*). However, this region is poorly ordered in the holo-RXRα LBD crystal structure (*11*).

A "mouse-trap" model of NR activation was proposed based on these structures (*12*), where binding of an agonist induced a unique active conformation that was favorable for recruitment of transcriptional coactivator complexes. However, other crystallographic studies suggested that the mechanism of NR activation was more complex than a simple two-state model. For example, the crystal structure of the RXRβ LBD with a bound synthetic agonist, LG268, was similar to the canonical structure of the apo-RXRα LBD structure with helix H12 in the extended position (*13*). The failure of LG268 to induce the canonical active conformation was partly attributed to packing forces within the crystal lattice. This observation also suggested that RXR might differ from some other nuclear receptors in that helix H12 was more mobile and less influenced by ligand-binding alone.

Although recombinant human RXRα LBD (T223−T462) was crystallized as a monomer in the liganded form (*10*) and as a homotetramer in the unliganded form (*14*), in solution, it formed homodimers in the liganded form and both homodimers and tetramers in the unliganded form (*8*). Ligand-induced dissociation of RXRα tetramers could play an important role in RXRα activation (*15*−*18*). Analysis of the crystal structure of the RXRα LBD tetramer (*14*) revealed that helix H12 protruded from the core to bind the coactivator site of the adjacent subunit, thus physically excluding binding of coactivators and suggesting a mechanism for autorepression.

To probe the effect of ligands on the solution dynamics of the RXR LBD, we have initiated NMR studies of the recombinant human RXRα LBD (T223−T462). Among the various physical techniques, high-resolution NMR spectroscopy has the unique capacity to investigate dynamic properties of biomolecules over a range of time scales at atomic resolution (*19*). The recent development of the transverse relaxation-optimized spectroscopy (TROSY) (*20*) coupled with the deuterium-labeling strategy (*21*) has overcome the broadening line width problem traditionally associated with macromolecules. Therefore, it is now feasible to carry out protein backbone dynamics studies on macromolecules beyond 40 kDa, as demonstrated in the recent studies of the 82 kDa malate synthase (*22*, *23*) and 44 kDa trimeric chorismate mutase (*24*). We report here the chemical shift-based structure analysis and backbone ^{15}N relaxation studies of RXRα LBD (T223−T462).

MATERIALS AND METHODS

Expression of Isotopically Labeled Recombinant RXRα LBD (aa T223−*T462).* The expression vector was constructed using the polymerase chain reaction (*25*) and the template cDNA encoding hRXRα (*7*) to incorporate a 5′ *Nde*I site and a 3′ *Xho*I site in the fragment encoding amino acids 223−462. The cloned fragment was verified by DNA sequencing and then ligated into *Nde*I/*Xho*I-digested pET15b expression vector (Novagen, San Diego, CA). The BL21-(DE3) *Escherichia coli* bacteria (Invitrogen, Carlsbad, CA) transformed with the expression vector were grown in M9 medium in 99% D_2O (Cambridge Isotope Laboratories, Andover, MA) at 37 °C, supplemented with 1 g of $^{15}NH_4Cl$ (99% ^{15}N, Isotec, Miamisburg, OH) as the sole nitrogen source and either 4 g of U-$^{13}C_6$ (99%)-1,2,3,4,5,6-D_7 (97−98% D) glucose or 4 g of 1,2,3,4,5,6-D_7 (99% D) glucose (Cambridge Isotope Laboratories, Andover, MA) as the sole carbon source for either triple-labeled (U-[^{2}H,^{15}N,^{13}C]) or double-labeled (U-[^{2}H,^{15}N]) RXRα LBD. When the optical density at 600 nm in the culture reached 0.6, the incubation temperature was switched to 20 °C, and isopropyl-β-D-thiogalactopyranoside (IPTG) was added to a final concentration of 0.8 mM to induce protein expression. After a 48 h induction at 20 °C, the cells were harvested by centrifugation and stored at −80 °C.

The frozen cell paste was resuspended and lysed in lysis buffer (0.5 M NaCl and 20 mM Tris at pH 8.0), and the His_6-tagged RXRα LBD was purified on a TALON cobalt-Sepharose (Clontech, Mountain View, CA) column by washing with a buffer containing 15 mM imidazole, 0.5 M NaCl, and 20 mM Tris, pH 8.0, followed by elution with a buffer containing 125 mM imidazole, 0.5 M NaCl, and 20 mM Tris, pH 8.0. The eluted sample was digested with human α-thrombin (Haematologic Technologies, Essex Junction, VT) at 4 °C overnight to cleave off the His_6-tag. The cleaved protein was loaded on a HiLoad 26/60 Superdex 200 pg gel filtration column (Amersham Biosciences, Piscataway, NJ) at 4 °C and fractionated in either a reducing buffer (50 mM NaCl, 10 mM Tris, pH 8.0, 0.5 mM EDTA, and 10 mM β-mercaptoethanol) or a nonreducing buffer (500 mM NaCl, 10 mM Tris, pH 8.0) at 1.0 mL/min.

NMR Sample Preparation. Purified samples were concentrated from about 5−12 μM to 1.3 mM (monomer concentration, estimated using extinction coefficient $\epsilon = 16\,740$ $cm^{-1}\,M^{-1}$ at 280 nm) in Amicon ultrafiltration cells (Amicon Corp., Danvers, MA) at 4 °C and then exchanged in 2 mL of NMR buffer (20 mM potassium phosphate at pH 7.4, 50 mM KCl, 0.05% NaN_3, 0.5 mM EDTA, 8 mM β-mercaptoethanol, 5% D_2O) for 5 times. The final volume was 0.5 mL at 1 mM concentration. For the holo sample, more than 2-fold molar excess of the 12 mM stock of 9cRA (Sigma, St. Louis, MO) dissolved in DMSO-d_6 (Cambridge Isotope Laboratories, Inc., Andover, MA) was added to the 20 μM protein sample at ambient temperature midway through the concentration step. The addition and the rest of the preparation were carried out in the dark or very dim yellow light to avoid degradation of the light-sensitive 9cRA.

NMR Spectroscopy. For sequence-specific backbone resonance assignments, 4D TROSY-HNCOCA (*26*), 4D TROSY-$HNCO_{i-1}CA_i$ (*27*), 4D-TROSY-HNCACO (*26*), 4D ^{15}N,^{15}N-NOESY (*28*, *29*), 3D TROSY-HNCO (*30*, *31*), 3D TROSY-

HN(CA)CO (*32*), 3D TROSY-HNCACB (*26*, *31*), and 3D TROSY-HN(CO)CACB (*26*, *31*) were recorded on either 600 or 700 MHz four-channel Varian Inova spectrometers equipped with pulsed-field gradient triple resonance probes at 25 °C with parameters described in Supporting Information Table 1. Selection of the TROSY component in all experiments, the delay for the $^{13}C^{\alpha}-^{13}CO$ magnetization transfer in 3D HN(CA)CO, and the $^{13}C^{\beta}$ evolution time in 3D HN(CO)CACA and 3D HNCACB were carried out as described by Tugarinov and co-workers (*22*).

The combined chemical shift change upon ligand binding for a particular residue was calculated based on the weight factors determined using the BioMagResBank chemical shift database (*23*) using two equations. In eq 1 the contributions of all three chemical shifts were included:

$$\Delta\delta = \sqrt{(\Delta\delta_{HN})^2 + (0.341\Delta\delta_{N})^2 + (0.154\Delta\delta_{CO})^2} \quad (1)$$

In eq 2 the contribution of the amide proton was eliminated since it was more likely to be sensitive to neighboring effects of the bound ligand, and the resulting chemical shift perturbation was more likely to reflect changes in backbone ϕ/ψ dihedral angles:

$$\Delta\delta = \sqrt{(0.341\Delta\delta_{N})^2 + (0.154\Delta\delta_{CO})^2} \quad (2)$$

The ^{15}N T_1, $T_{1\rho}$, T_2, and steady-state $\{^1H\}-^{15}N$ NOE measurements were collected on the apo- and holo-U-[^2H,^{15}N]-enriched RXRα LBD homodimer using both conventional and TROSY-based experiments on a 500 MHz three-channel Varian Inova spectrometer equipped with a pulsed-field gradient triple resonance cryoprobe and a 700 MHz four-channel Varian Inova spectrometer equipped with pulsed-field gradient triple resonance probe at 25 °C. The TROSY T_1 experiments (*33*) were recorded with 16 transients, a 1.8 s interscan delay, and 7−10 relaxation delays between 10 ms and 3.0 s (e.g., 0.011(3), 0.059, 0.107, 0.161, 0.214, 0.321, 0.429, 0.857, 1.714, and 2.946 s). The conventional T_1 experiments (*34*) were recorded with 16 transients, a 2.4 s interscan delay, and 9 relaxation delays (0.010, 0.060(3), 0.110, 0.220, 0.340, 0.450, 0.620, 0.790, and 1.400 s). The TROSY T_2 experiments (*35*) were recorded with 16 transients, a 4.0 s interscan delay, 1 ms interval between consecutive ^{15}N refocusing pulses (the Carr−Purcell−Meiboom−Gill or CPMG spin−echo) at 4.39 kHz field strength, and 9 relaxation delays (0.002(2), 0.007, 0.012, 0.017, 0.022, 0.029, 0.037, 0.061, and 0.088 s). To detect exchange contribution to the transverse relaxation rate ($R_2 = 1/T_2$), the T_2 was also measured at zero B_1 field strength, i.e., without CPMG. The conventional non-TROSY $T_{1\rho}$ experiments (*36*, *37*) were recorded with 16 transients, a 2.4 s interscan delay, 1.56 kHz spin-lock field strength, and 10 relaxation delays (0.002, 0.004(3), 0.006, 0.008, 0.012, 0.015, 0.019, 0.033, 0.058, and 0.096 s). The TROSY (*33*) and non-TROSY (*34*) NOE experiments consisted of a pair of data sets recorded with 32 transients and a 7 s interscan delay, of which ^1H saturation was applied for the last 3 s in one data set. All NMR spectra were processed as previously described (*22*) using NMRPipe (*38*), and were analyzed with NMRView (*39*). Sequence-specific resonance assignments were aided with the program Seq_prob for amino acid type determination (*40*). The ^1H chemical shift was referenced externally to 2,2-dimethylsilapentane-5-sulfonic acid (DSS), and the ^{15}N and ^{13}C chemical shifts were indirectly referenced to DSS (*41*). Chemical shift indices were calculated from $^{13}C^{\alpha}$, $^{13}C^{\beta}$, and ^{13}CO chemical shifts using the CSI program (*42*) with the former two corrected for ^2H isotope effect (*43*). The T_1, $T_{1\rho}$, and T_2 values were calculated using Curvefit (http://cpmcnet.columbia.edu/dept/gsas/biochem/labs/palmer/software/curvefit.html), in which signal intensities at different relaxation delays were fit to a single-exponential function $I = I_0 \exp(-t/T)$, where $T = T_1$, $T_{1\rho}$, or T_2. The two-parameter fit employed in this program was used for the analysis of these relaxation experiments as described previously (*34*). The uncertainty in the measured intensity was estimated from either triplicate or duplicate measurements at a short relaxation delay. The non-TROSY T_2 value was then derived from the T_1 and $T_{1\rho}$ values using the following equation: $1/T_{1\rho} = \sin 2\theta/T_2 + \cos 2\theta/T_1$, where $\theta = \arctan(\omega_1/\Delta\omega)$, ω_1 is the resonance offset, and $\Delta\omega$ is the spin-lock field strength (*44*). The NOE value was calculated as the ratio of signal intensities with and without saturation, and the uncertainty was estimated by repeating the NOE experiments three times. The relaxation parameters for unresolved overlapping residues and with uncertainties larger than 40% were excluded from the analysis.

Rotational Diffusion Analysis. The T_1/T_2 ratios collected using conventional non-TROSY experiments were subjected to a filtering scheme using two criteria proposed by Tjandra *et al.* (*45*): (1) A residue with an NOE value lower than 0.65 was excluded. (2) A residue was also excluded if it met the following condition: $(\langle T_2\rangle - T_{2,j})/\langle T_2\rangle - (\langle T_1\rangle - T_{1,j})/\langle T_1\rangle = D_j > 1.5$ SD, where $T_{1,j}$ and $T_{2,j}$ are the T_1 and T_2 values of residue j, respectively, $\langle T_1\rangle$ and $\langle T_2\rangle$ are the average T_1 and T_2 values, respectively, and SD is the standard deviation from the average D_j value. As a result of the first criterion, residues A226−M230, K245−D263, G443−T445, and H459−T462 were excluded from the calculation. The rotational diffusion anisotropy was then calculated from the filtered T_1/T_2 ratios using the program Quadric_diffusion (http://cpmcnet.columbia.edu/dept/gas/biochem/labs/palmer/software/diffusion.html, ref *46*). The overall rotational correlation time τ_m was subsequently calculated from the trace of the diffusion tensor D_{iso} in the following: $\tau_m = 1/(6D_{iso})$. Since the accurate determination of rotational diffusion anisotropy requires a three-dimensional structure of the molecule, the crystal structures of apo-RXRα LBD (1LGD) (*10*) and the 9cRA-bound RXRα LBD in the PPARγ heterodimer complex (1FM6) (*47*) were chosen for the apo and holo data sets, respectively. We chose 1FM6 rather than the crystal structure of holo-RXRα LBD monomer (1FBY) (*11*) because residues P244−N262 were present in the former and not in the latter. The homodimeric interface in the crystal structure of RXRα LBD homo-tetramer (1G1U) (*14*) was used as the template for building the apo- and holo-homodimer. The principal moments of the inertia tensors for the crystal structure models were calculated using the program PDBinertia (http://cpmcnet.columbia.edu/dept/gas/biochem/labs/palmer/software/diffusion.html).

RESULTS

Purification of RXRα LBD Homodimer. The isotope-labeled recombinant His_6-tagged RXRα LBD (aa.T223−T462) was expressed and affinity-purified as described in

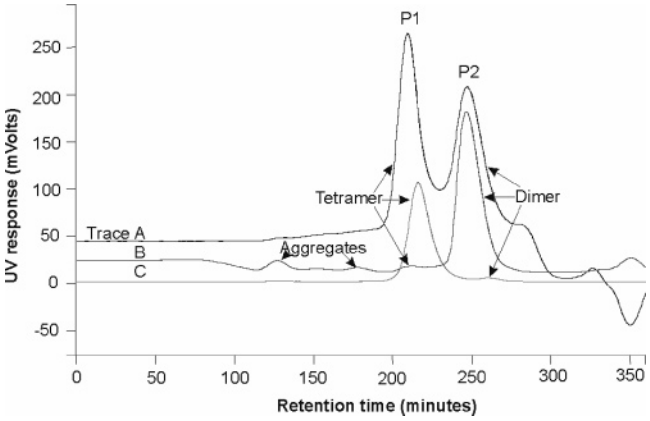

FIGURE 1: Reducing agents facilitated conversion of RXRα LBD tetramers to dimers. Three gel-filtration profiles of affinity purified, thrombin-digested apo-RXRα LBD fractionated over a Superdex 200-HR 26/60 gel filtration column at a flow rate of 1 mL/min are shown. Trace A: Affinity purified, thrombin-digested apo-RXRα LBD eluted with buffer containing 10 mM β-ME. Trace B: Pooled P2 (homodimer) fraction concentrated to 0.5 mL at 1 mM for NMR studies eluted with buffer containing 10 mM β-ME. Trace C: Pooled P1 (tetramer) fraction eluted with buffer without β-ME.

Materials and Methods. The His_6-tag was removed with human α-thrombin, leaving a tetrapeptide GSHM attached to the N-terminus T223, which was confirmed by the N-terminal protein sequencing. The digested RXRα LBD was fractionated over a Superdex 200 gel filtration column into two major fractions, P1 and P2 (see Figure 1). P1 corresponded to tetramers (MW 108 kDa), and P2 corresponded to dimers (MW 54 kDa), as confirmed by dynamic light scattering measurements of these two fractions. Rechromatography of the tetramer fraction in buffer containing β-mercaptoethanol (β-ME) or dithiothreitol (DTT) resulted in further conversion of tetramers to dimers (see Figure 1). Ultimately 80−90% of the protein was recovered as dimers after repeated gel-filtration chromatography of the tetramer fraction. Gel-filtration chromatography of an NMR sample of apo-RXRα LBD homodimer concentrated to 1 mM recovered 93% of the sample as dimer (see Figure 1), 5% as high molecular weight aggregates, and 2% as tetramer. Rechromatography of the RXRα LBD homodimer in the presence of 9cRA did not result in further dissociation to monomers. In the absence of a reducing agent, such as β-ME, the tetramer did not dissociate into dimer (see Figure 1), even when subjected to rechromatography in the presence of 9cRA (data not shown). Since electrospray mass spectometry of 40% of the RXRα LBD purified in the presence of DTT but not in the presence of β-ME showed a molecular mass that was 120 Da higher than expected (suggesting a possible covalent modification by DTT), all NMR experiments were conducted using buffers containing β-ME.

Sequence-Specific ^1HN, ^{15}N, $^{13}C^\alpha$, ^{13}CO, and $^{13}C^\beta$ Resonance Assignments. Since the RXRα LBD (T223−T462) monomer subunit consisted of 240 residues, 15 of which were proline residue, a maximum of 225 backbone amide $^1HN-^{15}N$ correlation peaks would be predicted in the HSQC spectra of the RXRα LBD homodimer, assuming that the resonances of the two subunits were degenerate. Due to the high helical content of the protein, there was severe signal overlap in the central region of the HSQC spectra of apo-

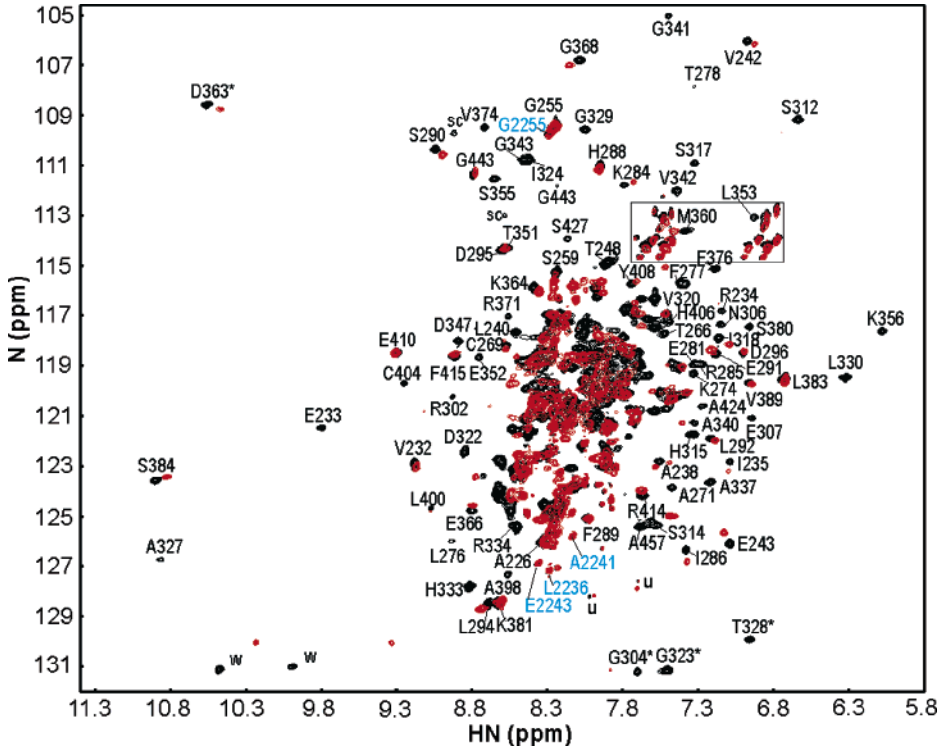

FIGURE 2: Superposition of $^1H-^{15}N$ TROSY-based heteronuclear single quantum correlation (HSQC) spectra for U-[^2H,^{15}N]-enriched apo-RXRα LBD (red) and holo-RXRα LBD complexed with 9cRA (black). The spectra were recorded on a 700 MHz spectrometer at 25 °C. The residue-specific assigned peaks in holo-RXRα LBD-9cRA complex were labeled according to the respective residue number in the protein sequence. Isolated peaks in the bound state are labeled with the amino acid one-letter code and the residue number, and the alias peaks are noted by an asterisk. The peaks stemming from the side chain groups are either enclosed in a rectangular box or labeled with the letters sc or w. Peaks likely from an unfolded/aggregate state are labeled with u. The minor set of peaks for residues N227−A252 and M254−N257 are labeled in cyan with the number 2 preceding the residue number.

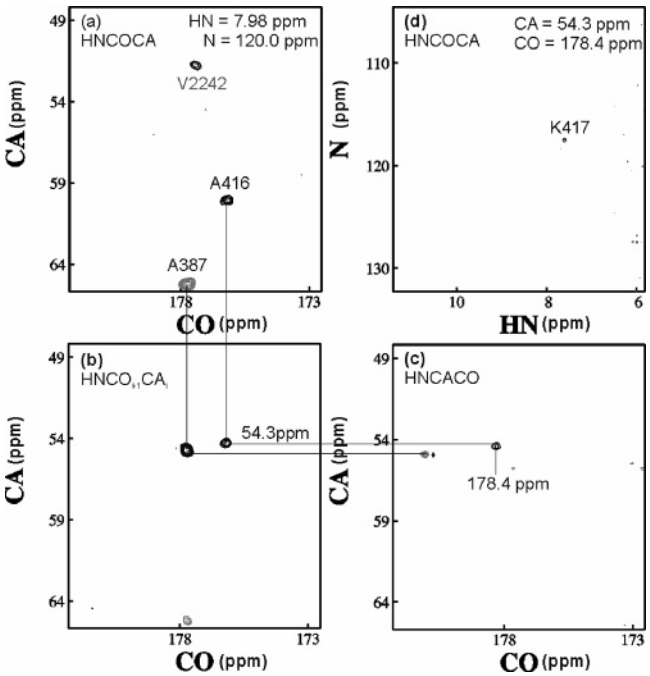

FIGURE 3: Sequence-specific backbone resonance assignments of F415−K417. (a−c) 2D Cα−CO planes of the three 4D TROSY-HNCOCA, $HNCO_{i-1}CA_i$, and HNCACO at amide HN and N chemical shifts of 7.98 and 120.0 ppm, respectively, showing correlations involving (a) HN_i, N_i, C^{α}_{i-1}, CO_{i-1}, (b) HN_i, N_i, C^{α}_i/C^{α}_{i-1}, CO_{i-1}, (c) HN_i, N_i, C^{α}_i, CO_i, where subscripts i and $i-1$ stand for the current (A416 and A387) and preceding residues, respectively. The two residues share the same amide HN and N chemical shift. The minor set of residue V242 also has similar amide chemical shifts, but the centers of the corresponding peaks are at a neighboring plane. (d) The 2D HN−N plane of the HNCOCA experiment at the Cα and CO chemical shifts of A416 showing its correlations with the amide HN and N of K417.

and holo-RXRα homodimer (see Figure 2). To overcome this problem, a series of TROSY 4D NMR (see Figure 3) as well as 3D NMR experiments (see Materials and Methods and Supporting Information Table 1) were carried out in order to separate the resonances. Sequence specific resonance assignments were made for 164 of 240 residues of the apo-RXRα subunit and 211 of 240 residues holo-RXRα subunit. The ^{1}HN, ^{15}N, $^{13}C^{\alpha}$, ^{13}CO, $^{13}C^{\beta}$ chemical shifts have been compiled in Supporting Information Table 2 and deposited in the BioMagResBank with accession numbers 6429 and 6449 for the apo- and holo-RXRα LBD, respectively. While most of the residues exhibited a single set of resonances for each residue, a second set of resonances with smaller intensities (<50%) was detected for residues N227−A252 and M254−N257 in both apo and holo proteins.

Secondary Structure Derived from Chemical Shift and NOE. The $^{13}C^{\alpha}$, ^{13}CO, and $^{13}C^{\beta}$ chemical shift differences between the measured and the random coil values for holo- and apo-RXRα LBD homodimers were calculated as described by Wishart and Sykes (*42*). As shown in Figure 4, residues V231−A241 showed large positive changes in the $^{13}C^{\alpha}$ and ^{13}CO chemical shifts, and were predicted to form an α-helix based on their calculated chemical shift index (*42*). The CSI-derived helical regions in both apo- and holo-RXRα LBD homodimer corresponded to helical regions observed in the crystal structures. Resonances corresponding to residues located in helices H3, H6, H10, H11, and H12 as well as the two β strands S1 and S2 in the crystal structure of the apo-RXRα LBD homodimer were missing in the spectra of the apo-RXRα LBD homodimer. The chemical shift indices of resonances corresponding to residues located in helices H2 and a portion of H12 in the spectra of the apo-RXRα homodimer did not predict a helical conformation. The chemical shift indices of residues corresponding to residue C269 in helix H3 of holo-RXRα LBD, and residues E352-L353 in helix H7 of both apo- and holo-RXRα LBD, also did not predict a helical conformation.

Resonances corresponding to residues located in portions of helices H10 and H11 in the crystal structure of the holo-RXRα LBD monomer were missing in the spectra of the holo-RXRα homodimer. Since incomplete exchange of amide deuterons for protons when the proteins were dissolved in H_2O could account for the remaining missing resonances, attempts were made to denature the protein followed by renaturing. However, very little functional protein was recovered. A partially deuterated holo-RXRα LBD homodimer sample was then prepared by expressing the protein in 50% D_2O. However, no additional signals were observed in the 3D HNCO spectrum, suggesting that the missing resonances were not due to incomplete deuteron amide exchange.

Analysis of the 4D ^{15}N,^{15}N-NOESY spectra recorded on U-[^{2}H,^{15}N]-enriched holo-RXRα LBD homodimer using a short mixing time (90 ms) revealed two symmetrical ^{1}HN−^{1}HN NOE cross-peaks between I324 and V332 (see Figure 5a,b) and L326 and L330 (data not shown), but no sequential ^{1}HN−^{1}HN NOE cross-peaks between these two pairs of residues. Since sequential NOE cross-peaks were associated with an upper limit of 4.8 Å (*48*), this suggested that the amide proton distances between I324 and V332 and between L326 and 330 were less than 4.8 Å. The detections of these NOE cross-peaks were consistent with the crystal structure of holo-RXRα LBD, where the interstrand (S1 and S2) backbone amide proton distances between the I324 and V332 and between L326 and L330 were 2.6 and 3.6 Å respectively (*11*).

Chemical Shift Perturbation Mapping. The weighted ^{1}HN, ^{15}N, and ^{13}CO chemical shift differences between resonances corresponding to 164 residues in apo- and holo-RXRα LBD were coded in a red-blue gradient and mapped on to the holo-RXRα LBD monomer crystal structure as shown in Figure 6. The largest chemical shift difference (~0.75 ppm mapped as red in the top panel) was observed at V349 in helix H7, followed by those for D347, T351, V354, and L350 in helix H7, E281, V280, and D263 in helix H3, E239 in helix H1, and L375 in helix H8. Moderate chemical shift differences (~0.2 ppm mapped as magenta in the top panel) were mapped to the residues in helices H1, H3, H4, H7, H8, and H12. Minimal chemical shift perturbations (<0.1 ppm mapped as blue in the top panel) were observed for residues in helices H5, H9, and H10. In order to probe structural changes in the protein upon ligand binding, we also recalculated the chemical shift perturbation after eliminating the amide proton contribution since these proton shifts were more sensitive to neighboring effects (*23*). Large chemical shift perturbations calculated without the amide proton component (≥0.2 ppm mapped as red in the bottom panel) were observed for D263, V280, and A283 in helix H3, E239 in helix H1, and F376 at the end of helix H8. Moderate chemical shift perturbations calculated without the amide

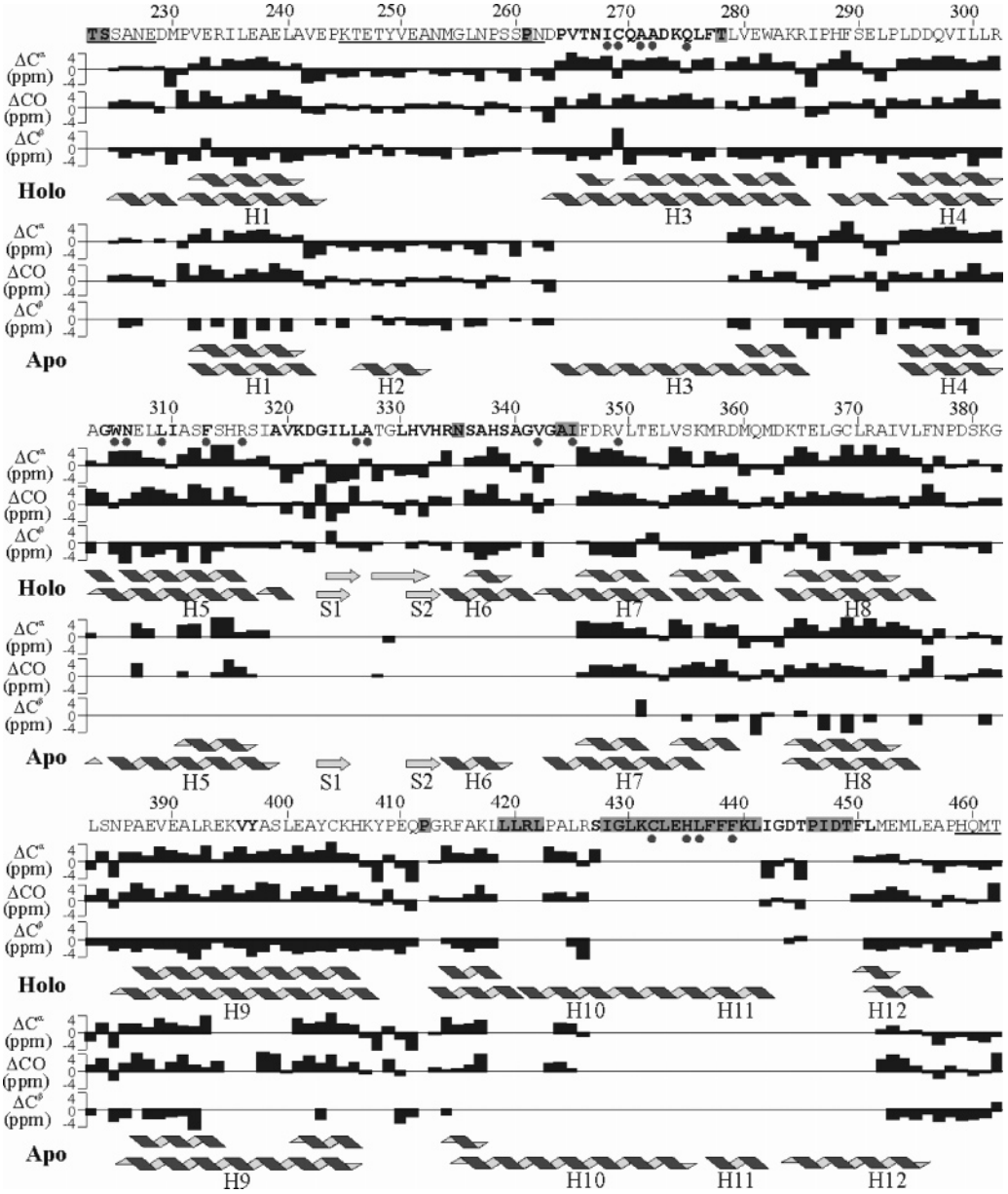

FIGURE 4: Chemical shift-based secondary structure of apo-RXRα LBD and holo-RXRα LBD−9cRA complex. The $^{13}C^{\alpha}$, ^{13}CO, and $^{13}C^{\beta}$ chemical shift differences between the measured and the random coil values are depicted in bar graphs for both holo- and apo-RXRα LBD under the primary sequence. The secondary structures derived from the chemical shift difference by the CSI program are depicted in ribbon diagrams (top) and compared with those in the crystal structures (bottom). The primary sequence is annotated in the following: The bold-faced and shaded letters are residues without resonance assignments in apo- and holo-RXRα LBD, respectively; the ones marked by filled circles are residues in direct contact with 9cRA in the crystal structure; and the underlined ones are residues without electron densities in the crystal structures.

proton component (0.17−0.2 ppm mapped as magenta in the bottom panel) were observed for E453 and M454 in helix H12 and E281 in helix H3.

Resonances corresponding to 47 residues primarily located in helices H3 and H5 and strands S1 and S2 emerged upon 9cRA-binding (mapped as orange in Figure 6). In addition resonances corresponding to residues V396−A398 in helix H9 also emerged upon 9cRA-binding. As described above, resonances corresponding to 29 residues mapped primarily to helices H10 and H11 as well as the H11−H12 loop (mapped as yellow in Figure 6) were undetectable in the spectra of both apo- and holo-RXRα LBD.

^{15}N T_1, T_2, and Steady-State $\{^1H\}-^{15}N$ NOE Data. To probe the backbone dynamics of RXRα LBD, the ^{15}N longitudinal (T_1) and transverse (T_2) relaxation times as well as steady-state $\{^1H\}-^{15}N$ nuclear Overhauser effect (NOE) were measured on apo- and holo-[^2H,^{15}N]-enriched RXRα LBD at both 500 and 700 MHz static magnetic fields using conventional non-TROSY-based experiments and TROSY-based experiments. Due to problems of signal overlaps and weak signal intensities in the conventional experiments, complete T_1, T_2 data sets were obtained for only 35 residues in apo-RXRα LBD and 100 residues in holo-RXRα LBD at both magnetic fields (see Figure 7). In contrast to the T_1 and T_2 measurements for some of the residues in the H1−H3 loop (K245−D263) of both apo- and holo-RXRα LBD and the residues in the H11−H12 loop (G443−T445) of holo-RXRα LBD, the respective heteronuclear NOEs could not be measured, probably because the expected values were close to zero. The average estimated errors for T_1, T_2, and

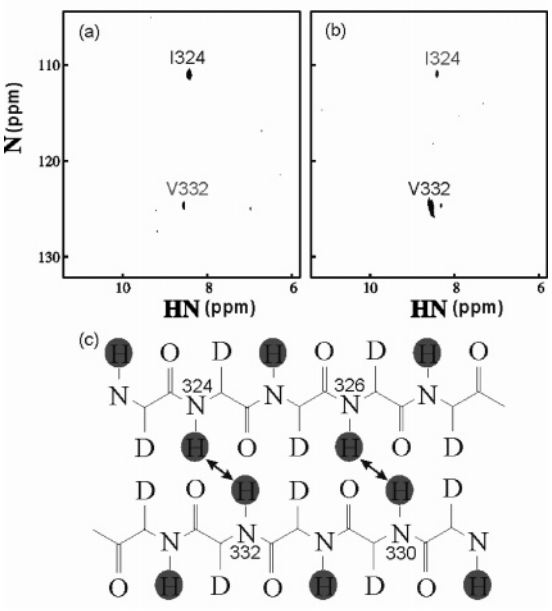

FIGURE 5: NOE-derived antiparallel β-sheet. (a and b) The amide HN−N planes of a 4D ^{15}N,^{15}N-NOESY spectrum of holo-hRXRα LBD−9cRA complex collected at 700 MHz, at the amide HN and N chemical shifts of residues I324 (8.42 ppm, 110.9 ppm) and V332 (8.56 ppm, 124.6 ppm), respectively. (c) The structure of the antiparallel β-sheet and the observed long-range interproton NOEs (double arrows). The labile amide protons are in shaded circles to be distinguished from the nonlabile deuterons.

heteronuclear NOE values were 8%, 12%, and 10% respectively. Since the T_1, T_2, and heteronuclear NOE values were sensitive to the backbone motion on the ps−ns time scale, a qualitative assessment of the protein internal motion could be made. As shown in Figure 7, the internal motions for the residues located at the N-terminus (A226−M230), the H1−H3 loop (K245−D263), the H11−H12 loop (G443−T445), and the C-terminus (A457−T462) were clearly different from the rest of the protein in both the apo- and holo-form because of their distinct T_1, T_2, and heteronuclear NOE values. The relaxation parameters for the majority of the 35 residues in apo-RXRα LBD, including the residues in the AF-2 helix and the C-terminal region of the protein (M454−T262), did not show significant changes upon 9cRA binding. The T_2 value for D263 was consistently higher for apo-RXRα LBD than for holo-RXRα LBD in all of the data sets.

Since the TROSY-based experiments could offer higher resolution and sensitivity than the conventional experiments (*20*), the T_1, T_2, and heteronuclear NOE values were also measured using TROSY experiments on the same samples. As predicted based on theoretical considerations (*20*), the overall T_1, T_2, and NOE values measured using TROSY experiments were significantly higher than those measured using non-TROSY experiments, and the difference was larger at 700 MHz than at 500 MHz (Supplemental Figure 1, Supporting Information). However the relaxation data obtained using TROSY and non-TROSY experiments exhibited similar patterns of variation along the polypeptide chain.

Rotational Diffusion Analysis. The hydrodynamic properties of the molecule can be characterized by rotational diffusion analysis of the T_1 and T_2 parameters. All quantitative analyses described in this section were carried out using only the conventional non-TROSY data sets since the theoretical framework is well established and programs for analyzing these measurements are widely available (*46*). The T_1/T_2 ratios were fitted to the isotropic, axially symmetric and asymmetric models using the program Quadric_diffusion as described in Materials and Methods. The principal moments of inertia tensors for the apo and holo homodimer structures used in this analysis were (1.00, 0.93, 0.42) and (1.00, 0.90, 0.64), respectively, indicative of slight axial anisotropy. However, the results of the rotational diffusion analysis showed no statistical significance of the axially symmetric model over the isotropic model except for the case of holo data set at the 700-MHz static magnetic field, and no statistical significance of the anisotropic model over the axially symmetric model in all cases. This was probably because of the limited size of the data sets and the relatively large uncertainties of the measured parameters for some residues. Therefore, only the result for the isotropic model is presented in Table 1. The overall rotational correlation times, τ_m, were 24.5 ns at 500 MHz and 16.8 ns at 700 MHz for apo-RXRα LBD and 26.1 ns at 500 MHz and 19.1 ns at 700 MHz for holo-RXRα LBD. The rotational correlation times are considerably longer than the correlation times predicted for a monomer, 13 ns, and shorter than the correlation time predicted for a tetramer, >40 ns, based on a comparison with other proteins (see Figure 8). These measurements confirm that the predominant form of the RXRα LBD in the NMR sample is a homodimer.

Measurement of the ^{15}N Transverse Relaxation Rate R_2 at Two Static B1 Fields. Conformational exchange on the micro- to millisecond time scale results in a contribution to the effective transverse relaxation rate, termed R_{ex}. Applying different B_1 field strengths in the form of the CPMG pulse sequence during the transverse relaxation delay could attenuate such exchange contribution (*54*). The transverse relaxation rates R_2 were measured in the TROSY-CPMG experiments using both 1000 and 0 Hz B_1 field strengths on the 500 and 700 MHz spectrometers. The R_2 differences with 40% error or less were plotted against the residue numbers for both apo- and holo-RXRα LBD, as shown in Figure 9. Significant R_2 differences at the two B1 fields were observed for residues in helices H1, H2, H4, H7, H8, and H10 as well as the H8−H9 loop of apo-RXRα LBD, indicating that these residues sensed exchange processes on the micro- to millisecond time scale. Of note, significant R_2 differences were also observed for residues in helices H1, H3, H4, H5, H7, H8, H9, H10, and H12, the H1−H3, H8−H9, and H11−H12 loops, and the β-hairpin of holo-RXRα LBD. Since the exchange contribution increased from the 500 to 700 MHz static magnetic field strength for residues E239, T248, V250, K381, L383, A457, and M461 of holo-RXRα LBD, the exchange rates for these residues were larger than the chemical shift difference between the two exchange sites (*54*).

DISCUSSION

A number of changes in the NMR spectra of the RXRα LBD were observed with 9cRA binding. Some changes simply reflect proximity of residues within the binding pocket to the bound 9cRA, such as the chemical shift perturbations mapped to V349 and neighboring residues in helix H7. Other changes likely reflect changes in protein conformation previously observed in the crystal structures of apo- and holo-RXRα LBD (*10*, *11*), such as the ligand-induced chemical

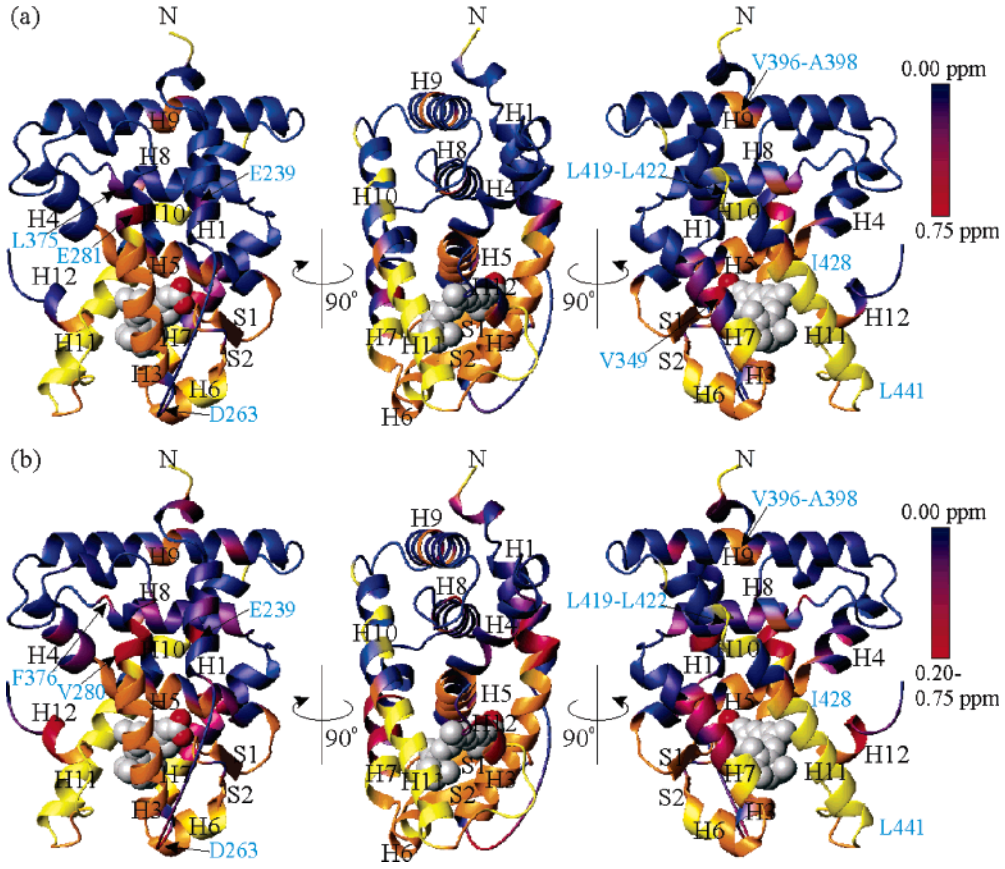

FIGURE 6: Chemical shift perturbation mapping. The root-mean-squared weighted (a) ^{1}HN, ^{15}N, and ^{13}CO chemical shift differences and (b) ^{15}N and ^{13}CO chemical shift differences between the bound and unbound states are coded in a blue-to-red gradient with either the maximal difference (a) or 0.2 ppm (b) as the upper bound and mapped onto the crystal structure of human RXRα LBD bound to 9cRA. Residues unassigned in both the bound and unbound states are yellow, and those unassigned only in the unbound state are orange. The left and right panels resulted from a 90° vertical turn of the middle ones. The images were generated from MOLMOL v.2k.1.

shift perturbations mapped to regions outside the binding pocket in helices H3 and H12.

The most striking effect of 9cRA binding on the NMR spectra of RXRα LBD (T223−T462) was the emergence of an additional 47 cross-peaks. The majority of these cross-peaks corresponded to residues that were located within the ligand-binding pocket in the crystal structures of holo-RXRα LBD. The emergence of cross-peaks for residues V396−A398 in helix H9 suggested that 9cRA binding had allosteric effects on the dimerization interface, since Y397 in helix H9 from one subunit of crystalline apo-RXRα homodimer was in contact with residue L420 in helix H10 from the partnering subunit.

The emergence of missing cross-peaks was previously observed in the NMR spectra of the PPARγ and PPARα LBDs upon binding agonist (*55*, *56*). However, in contrast to the PPARγ LBD, residues in the N-terminal part of helix H7, parts of helix H10 and helix H11 in RXRα LBD remained undetectable after ligand binding. This was somewhat surprising, since residue I345 in helix H7 and residues C432, H435, L436, and F439 in helices H10 and H11 were in contact with bound 9cRA in the crystal structure of holo-RXRα LBD.

Missing cross-peaks in NMR spectra could arise from a number of causes, including cross-peak overlap, incomplete deuteron amide exchange, or exchange peak broadening. Incomplete deuteron exchange in this region was unlikely since previous studies demonstrated deuteron exchange in this region (*57*). Furthermore, reducing the deuterium enrichment of the recombinant RXRα LBD did not result in the appearance of any additional cross-peaks. The more likely explanation was that peak intensities of these missing residues were reduced by line broadening because of chemical exchange. The chemical exchange processes accounting for the missing cross-peaks in the spectra of PPARγ LBD reflected only conformational exchange within the subunit, since the PPARγ LBD was a monomer. Although gel-filtration chromatography and measurement of the rotational correlation time indicated that apo- and holo-RXRα LBD were predominantly in the dimeric form, this did not exclude ongoing association and dissociation of the RXRα LBD subunits to form monomers and tetramers. Missing cross-peaks corresponding to residues in helices H10 and H11, which participate in the dimeric and tetrameric interfaces, could reflect intersubunit rather than intrasubunit exchange processes. Further dissection of intrasubunit from intersubunit exchange processes could be approached by analysis of mutant RXRα LBD proteins with altered oligomerization properties (*18*, *58*).

On the other hand, cross-peaks corresponding to T246−A252 were detectable in the NMR spectra of both the apo- and holo-RXRα LBDs. This region formed helix H2 in the crystal structure of the apo-RXRα homodimer (*10*), but was poorly defined in the crystal structure of the holo-RXRα

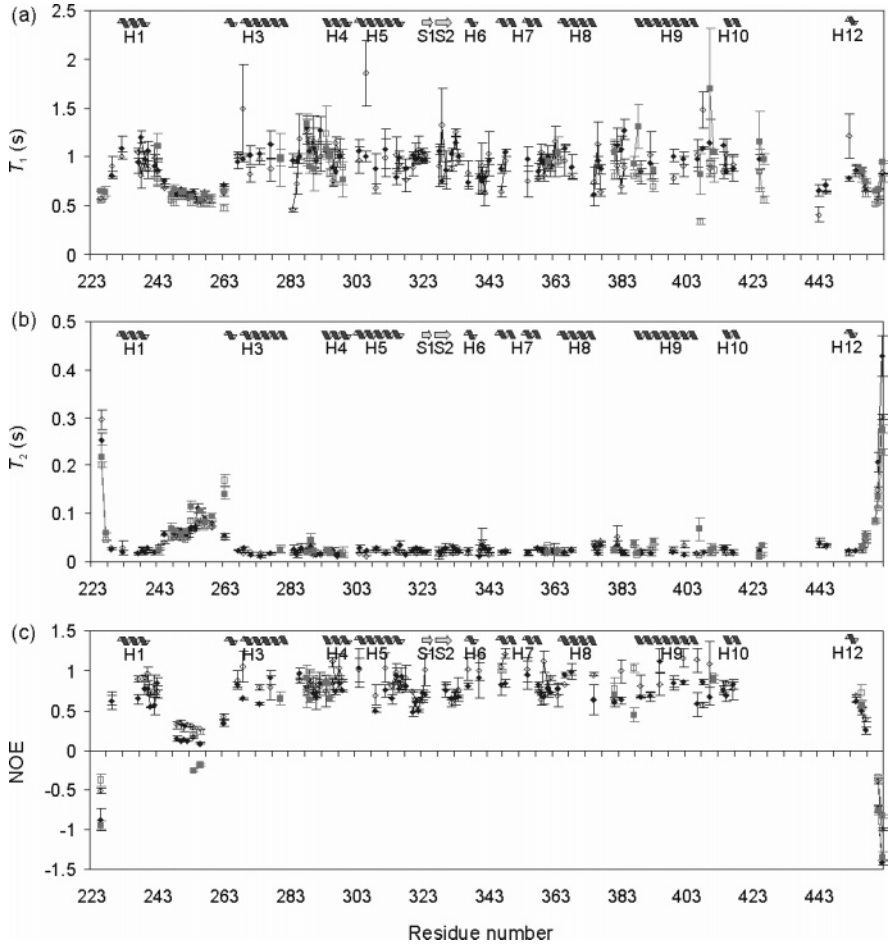

FIGURE 7: Histograms of ^{15}N T_1, T_2 and steady-state $\{^1H\}-^{15}N$ NOE measurements on U-[^2H,^{15}N]-enriched RXRα LBD with (dark filled and hollow diamonds) and without (gray filled and hollow squares) 9cRA. The measurements were collected using the conventional non-TROSY-based pulse sequences at 500 MHz (filled diamonds and squares) and 700 MHz (hollow diamonds and squares) static magnetic field strengths at 25 °C. The ribbon diagrams of the chemical shift-based secondary structure of holo-RXRα LBD were drawn on the top of each panel.

Table 1: Rotational Diffusion Tensors for RXRα LBD at 25 °C[a]

	apo		holo	
	500 MHz	700 MHz	500 MHz	700 MHz
τ_m (ns)	24.5 ± 0.6	16.8 ± 0.3	26.1 ± 0.3	19.1 ± 0.2
χ^2	185	144	146	537
data points[b]	17	25	57	54

[a] The result was obtained from the Quadric_diffusion program. [b] A number of T_1/T_2 ratios failed in the minimization procedure due to their relatively large errors and were excluded in the final calculation.

monomer (*11*). The T_1, T_2, and heteronuclear NOE values for the H1−H3 loop differed significantly from the rest of the polypetide chain in both apo- and holo-RXRα LBD. The apparent field dependence of the overall rotational correlation times indicated that the approximation of fast internal dynamics ($\tau_e \ll \tau_m$) did not hold. For this reason, the Lipari−Szabo formalism was not applied to calculate a generalized order parameter, S_2. However, qualitative inspection of the relaxation parameters indicated that the backbone dynamics on the pico- to nanosecond time scale was less restricted in the H1−H3 loop compared to the rest of the polypeptide chain in both apo- and holo-RXRα LBD. Because this region of the protein is not involved in intersubunit interactions, the relaxation parameters measured for this region of the protein probably reflected motions within the LBD subunit.

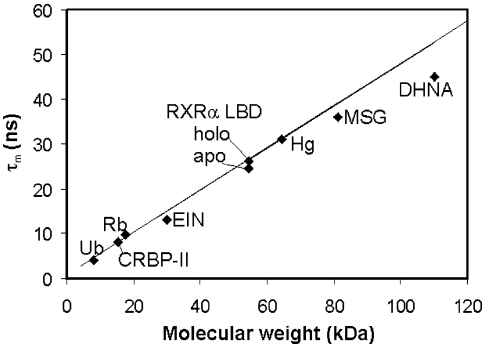

FIGURE 8: RXRα LBD correlation time τ_m and estimated molecular weight. The linear relationship (r^2 = 0.999) between τ_m and molecular weight was derived from four proteins reported in the literature (*45*−*51*), including ubiquitin (Ub, 8.0 kDa, 4.16 ns, 27 °C), cellular retinol-binding protein II (CRBP II, 15.5 kDa, 8.1 ns, 25 °C), ribonuclease HI (Rb, 17.6 kDa, 9.7 ns, 27 °C), and hemoglobin (Hg, 64.5 kDa, 31.2 ns, 29 °C). The temperature effect on the τ_m values was not corrected. Three proteins (*22*, *52*, *53*) including enzyme I N-domain (EIN, 30 kDa, 13.1 ns, 40 °C), malate synthase G (MSG, 81.4 kDa, 36.1 ns, 37 °C), and 7,8-dihydroneopterin aldolase (DHNA, 110 kDa, 45 ns, 20 °C), provide additional reference points.

Conclusions on the effect of 9cRA on backbone dynamics were limited by missing cross-peaks corresponding to helices H3, H6, H10, H11, and H12 as well as the two β strands S1

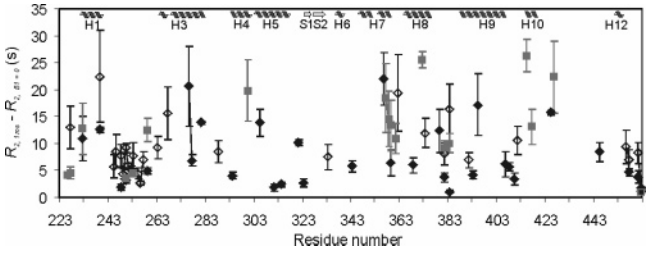

FIGURE 9: Probing the chemical or conformational exchange on the μs−ms time scale. The differences between the transverse relaxation rates measured at 1000 and 0 Hz B_1 field strengths on both 500 MHz (filled diamonds and squares) and 700 MHz (hollow diamonds and squares) spectrometers are plotted against the residue numbers for both apo-RXRα LBD (gray squares) and holo-RXRα LBD (dark diamonds). The error bar was calculated from the errors of the R_2 values according to the propagation rule.

and S2 in the apo-RXRα LBD spectra. Binding of 9cRA appeared to lower the T_2 value of D263 in the H1−H3 loop, suggesting that this residue sensed ligand induced alterations in backbone dynamics. Although the prevailing model for ligand-activation predicted that the H12 (AF-2) helix would be locked into an activated conformation with reduced mobility, binding of 9cRA appeared to have minimal effect on the relaxation parameters corresponding to the C-terminal residues of the RXRα LBD. Previous fluorescence anisotropy experiments demonstrated that ligand binding restricted the conformational mobility of the C-terminus of PPARγ on the pico- to nanosecond time scale (*59*). In contrast, our NMR studies indicated that the RXRα LBD C-terminus sensed exchange processes on the pico- to nanosecond time scale even after binding of 9cRA.

To initially probe the effect of 9cRA on backbone dynamics on the micro- to millisecond time scale, we measured the transverse relaxation rate, R_2, at two B1 fields. Significant R_2 differences were measured for residues located throughout the polypeptide chain for holo-RXRα LBD, suggesting that these residues were sensing exchange processes on the micro- to millisecond time scale. In contrast, binding of *all-trans*-retinol to cellular retinol binding protein (CRBP) I and II resulted in flat relaxation dispersion profiles in almost all of the residues (*49*). Thus, while binding of ligand suppressed conformational exchange processes on a micro- to millisecond time scale in CRBP I and CRBP II, this did not appear to be the case for the RXRα LBD. Whether the exchange processes observed for holo-RXRα LBD reflected intra- or intersubunit exchange processes remained to be determined.

Taken together our studies indicate that the RXRα LBD exists as a dynamic ensemble of conformations, even after binding its cognate ligand. Such dynamic characteristics may allow RXRα to partner with multiple nuclear receptors.

ACKNOWLEDGMENT

We thank Mr. Liang Zhang and Dr. Xueping E for their advice on RXRα LBD cloning, Professor Lewis Kay and Dr. Vitali Tugarinov for providing the 4D pulse sequences and NMRPipe processing scripts, Professor Arthur Palmer, III, for providing the Curvefit, Quadric_diffusion and PDBinertia programs, and Professor Kathleen Hall for many helpful discussions.

SUPPORTING INFORMATION AVAILABLE

NMR data and NOE measurements. This material is available free of charge via the Internet at http://pubs.acs.org.

REFERENCES

1. Chawla, A., Repa, J. J., Evans, R. M., and Mangelsdorf, D. J. (2001) Nuclear receptors and lipid physiology: opening the X-files, *Science 294*, 1866−70.
2. Cao, X., Liu, W., Lin, F., Li, H., Kolluri, S. K., Lin, B., Han, Y.-H., Dawson, M. I., and Zhang, X.-K. (2004) Retinoid X receptor regulates Nur77/thyroid hormone receptor 3-dependent apoptosis by modulating its nuclear export and mitochondrial targeting, *Mol. Cell. Biol. 24*, 9705−25.
3. Dezube, B. J., Pantanowitz, L., and Aboulafia, D. M. (2004) Management of AIDS-related Kaposi sarcoma: advances in target discovery and treatment, *AIDS Read. 14*, 236−8, 243−4, 251−3.
4. Knobler, E. (2004) Current management strategies for cutaneous T-cell lymphoma, *Clin. Dermatol. 22*, 197−208.
5. Hede, K. (2004) Retinoids may be ready for prime time in prevention, but challenges remain, *J. Natl. Cancer Inst. 96*, 1807−8.
6. Yamauchi, T., Waki, H., Kamon, J., Murakami, K., Motojima, K., Komeda, K., Miki, H., Kubota, N., Terauchi, Y., Tsuchida, A., Tsuboyama-Kasaoka, N., Yamauchi, N., Ide, T., Hori, W., Kato, S., Fukayama, M., Akanuma, Y., Ezaki, O., Itai, A., Nagai, R., Kimura, S., Tobe, K., Kagechika, H., Shudo, K., and Kadowaki, T. (2001). Inhibition of RXR and PPARgamma ameliorates diet-induced obesity and type 2 diabetes, *J. Clin. Invest. 108*, 1001−13.
7. Cheng, L., Norris, A. W., Tate, B. F., Rosenberger, M., Grippo, J. F., and Li, E. (1994) Characterization of the ligand binding domain of human retinoid X receptor alpha expressed in Escherichia coli, *J. Biol. Chem. 269*, 18662−7.
8. Egea, P. F., Rochel, N., Birck, C., Vachette, P., Timmins, P. A., and Moras, D. (2001) Effects of ligand binding on the association properties and conformation in solution of retinoic acid receptors RXR and RAR, *J. Mol. Biol. 307*, 557−76.
9. Chen, Z.-P., Iyer, J., Bourguet, W., Held, P., Mioskowski, C., Lebeau, L., Noy, N., Chambon, P., and Gronemeyer, H. (1998) Ligand- and DNA-induced dissociation of RXR tetramers, *J. Mol. Biol. 275*, 55−65.
10. Bourguet, W., Ruff, M., Chambon, P., Gronemeyer, H., and Moras, D. (1995) Crystal structure of the ligand-binding domain of the human nuclear receptor RXR-alpha, *Nature 375*, 377−82.
11. Egea, P. F., Mitschler, A., Rochel, N., Ruff, M., Chambon, P., and Moras, D. (2000) Crystal structure of the human RXRalpha ligand-binding domain bound to its natural ligand: 9-cis retinoic acid, *EMBO J. 19*, 2592−601.
12. Wurtz, J. M., Bourguet, W., Renaud, J. P., Vivat, V., Chambon, P., Moras, D., and Gronemeyer, H. (1996) A canonical structure for the ligand-binding domain of nuclear receptors, *Nat. Struct. Biol. 3*, 206.
13. Love, J. D., Gooch, J. T., Benko, S., Li, C., Nagy, L., Chatterjee, V. K., Evans, R. M., and Schwabe, J. W. (2002) The structural basis for the specificity of retinoid-X receptor-selective agonists: new insights into the role of helix H12, *J. Biol. Chem. 277*, 11385−91.
14. Gampe, R. T., Jr., Montana, V. G., Lambert, M. H., Wisely, G. B., Milburn, M. V., and Xu, H. E. (2000) Structural basis for autorepression of retinoid X receptor by tetramer formation and the AF-2 helix, *Genes Dev. 14*, 2229−41.
15. Kersten, S., Pan, L., Chambon, P., Gronemeyer, H., and Noy, N. (1995). Role of ligand in retinoid signaling. 9-cis-retinoic acid modulates the oligomeric state of the retinoid X receptor, *Biochemistry 34*, 13717−21.
16. Lin, B. C., Wong, C. W., Chen, H. W., and Privalsky, M. L. (1997). Plasticity of tetramer formation by retinoid X receptor. An alternative paradigm for DNA recognition, *J. Biol. Chem. 272*, 9860−7.
17. Kersten, S., Gronemeyer, H. and Noy, N. (1997) The DNA binding pattern of the retinoid X receptor is regulated by ligand-dependent modulation of its oligomeric state, *J. Biol. Chem. 272*, 12771−7.
18. Kersten, S., Reczek, P. R., and Noy, N. (1997) The tetramerization region of the retinoid X receptor is important for transcriptional activation by the receptor, *J. Biol. Chem. 272*, 29759−68.

19. Palmer, A. G., 3rd, Kroenke, C. D., and Loria, J. P. (2001) Nuclear magnetic resonance methods for quantifying microsencond-to-millisecond motions in biological macromolecules, *Methods Enzymol. 339*, 204−38.
20. Pervushin, K., Riek, R., Wider, G., and Wüthrich, K. (1997) Attenuated T2 relaxation by mutual cancellation of dipole−dipole coupling and chemical shift anisotropy indicates an avenue to NMR structures of very large biological macromolecules in solution, *Proc. Natl. Acad. Sci. U.S.A. 94*, 12366−71.
21. Gardner, K. H., and Kay, L. E. (1998) The use of ^{2}H, ^{13}C, ^{15}N multidimensional NMR to study the structure and dynamics of proteins, *Annu. Rev. Biophys. Biomol. Struct. 27*, 357−406.
22. Tugarinov, V., Muhandiram, R., Ayed, A., and Kay, L. E. (2002) Four-dimensional NMR spectroscopy of a 723-residue protein: chemical shift assignments and secondary structure of malate synthase G, *J. Am. Chem. Soc. 124*, 10025−35.
23. Tugarinov, V., and Kay, L. E. (2003) Quantitative NMR studies of high molecular weight proteins: application to domain orientation and ligand binding in the 723 residue enzyme malate synthase G, *J. Mol. Biol. 327*, 1121−33.
24. Eletsky, A., Kienhofer, A., Hilvert, D., and Pervushin, K. (2005). Investigation of ligand binding and protein dynamics in Bacillus subtilis chorismate mutase by transverse relaxation optimized spectroscopy−nuclear magnetic resonance, *Biochemistry 44*, 6788−99.
25. Saiki, R., Gelfand, D. H., Stoffel, S., Scharf, S. J., Higuchi, R., Horn, G. T., Mullis, K. B., and Erlich, H. A. (1988) Primer-directed enzymatic amplification of DNA with a thermostable DNA polymerase, *Science 239*, 487−8.
26. Yang, D., and Kay, L. E. (1999) TROSY triple-resonance four-dimensional NMR spectroscopy of a 46 ns tumbling protein, *J. Am. Chem. Soc. 121*, 2571−5.
27. Konrat, R., Yang, D., and Kay, L. E. (1999). A 4D TROSY-based pulse scheme for correlating ^{1}HN$_i$,^{15}N$_i$,^{13}Cα_i,^{13}C$'_{i-1}$ chemical shifts in high molecular weight, ^{15}N, ^{13}C, ^{2}H labeled proteins, *J. Biomol. NMR 15*, 309−13.
28. Venters, R. A., Metzler, W. J., Spicer, L. D., Mueller, L., and Farmer, B. T. J. (1995) Use of ^{1}HN-^{1}HN NOEs to determine protein global folds in perdeuterated proteins, *J. Am. Chem. Soc. 117*, 9592−3.
29. Grzesiek, S., Wingfield, P., Stahl, S., Kaufman, J. D., and Bax, A. (1995) Four-dimensional ^{15}N-separated NOESY of slowly tumbling perdeuterated ^{15}N-enriched proteins. Application to HIV-1 nef, *J. Am. Chem. Soc. 117*, 9594−5.
30. Yang, D., and Kay, L. E. (1999) Improved ^{1}HN-detected triple resonance TROSY-based experiments, *J. Biomol. NMR 13*, 3−10.
31. Salzmann, M., Pervushin, K., Wider, G., Senn, H., and Wüthrich, K. (1998) TROSY in triple-resonance experiments: new perspectives for sequential NMR assignment of large proteins, *Proc. Natl. Acad. Sci. U.S.A. 95*, 13585−90.
32. Clubb, R. T., Thanabal, V., and Wagner, G. (1992) A constant-time three-dimensional triple-resonance pulse scheme to correlate intraresidue ^{1}HN, ^{15}N, and ^{13}C′ chemical shifts in ^{15}N-^{13}C-labeled proteins, *J. Magn. Reson. 97*, 213−7.
33. Zhu, G., Xia, Y., Nicholson, L. K., and Sze, K. H. (2000) Protein Dynamics Measurements by TROSY−Based NMR Experiments, *J. Magn. Reson. 143*, 423−6.
34. Farrow, N. A., Muhandiram, R., Singer, A. U., Pascal, S. M., Kay, C. M., Gish, G., Shoelson, S. E., Pawson, T., Forman-Kay, J. D., and Kay, L. E. (1994) Backbone dynamics of a free and phosphopeptide-complexed Src homology 2 domain studied by ^{15}N NMR relaxation, *Biochemistry 33*, 5984−6003.
35. Loria, J. P., Rance, M., and Palmer, A. G. (1999) A TROSY CPMG sequence for characterizing chemical exchange in large proteins, *J. Biomol. NMR 15*, 151−5.
36. Korzhnev, D. M., Skrynnikov, N. R., Millet, O., Torchia, D. A., and Kay, L. E. (2002) An NMR experiment for the accurate measurement of heteronuclear spin-lock relaxation rates, *J. Am. Chem. Soc. 124*, 10743−53.
37. Tugarinov, V., Choy, W.-Y., Kupèe, E., and Kay, L. E. (2004) Addressing the overlap problem in the quantitative analysis of two-dimensional NMR spectra: application to (15)N relaxation measurements, *J. Biomol. NMR 30*, 347−52.
38. Delaglio, F., Grzesiek, S., Vuister, G. W., Zhu, G., Pfeifer, J., and Bax, A. (1995) NMRPipe: a multidimensional spectral processing system based on UNIX pipes, *J. Biomol. NMR 6*, 277−93.
39. Johnson, B. A., and Blevins, R. A. (1994) NMRView: A computer program for the visualization and analysis of NMR data, *J. Biomol. NMR 4*, 603−14.
40. Grzesiek, S., and Bax, A. (1993) Amino acid type determination in the sequential assignment procedure of uniformly ^{13}C/^{15}N-enriched proteins, *J. Biomol. NMR 3*, 185−204.
41. Markley, J. L., Bax, A., Arata, Y., Hilbers, C. W., Kaptein, R., Sykes, B. D., Wright, P. E., and Wüthrich, K. (1998) Recommendations for the presentation of NMR structures of proteins and nucleic acids, *Pure Appl. Chem. 70*, 117−42.
42. Wishart, D. S., and Sykes, B. D. (1994) The ^{13}C chemical-shift index: a simple method for the identification of protein secondary structure using ^{13}C chemical-shift data, *J. Biomol. NMR 4*, 171−80.
43. Gardner, K. H., Rosen, M. K., and Kay, L. E. (1997). Global folds of highly deuterated, methyl-protonated proteins by multidimensional NMR, *Biochemistry 36*, 1389−401.
44. Peng, J., and Wagner, G. (1992) Mapping of spectral density functions using heteronuclear NMR relaxation measurements, *J. Magn. Reson. 98*, 308−32.
45. Tjandra, N., Feller, S. E., Paster, R. W., and Bax, A. (1995) Rotational diffusion anisotropy of human ubiquitin from ^{15}N NMR relaxation, *J. Am. Chem. Soc. 117*, 12562−6.
46. Lee, L. K., Rance, M., Chazin, W. J., and Palmer, A. G. (1997) Rotational diffusion anisotropy of proteins from simultaneous analysis of ^{15}N and ^{13}C$^{\alpha}$ nuclear spin relaxation, *J. Biomol. NMR 9*, 287−98.
47. Gampe, R. T., Jr., Montana, V. G., Lambert, M. H., Miller, A. B., Bledsoe, R. K., Milburn, M. V., Kliewer, S. A., Willson, T. M., and Xu, H. E. (2000) Asymmetry in the PPARgamma/RXRalpha crystal structure reveals the molecular basis of heterodimerization among nuclear receptors, *Mol. Cell 5*, 545−55.
48. Wüthrich, K. (1986) *NMR of Proteins and Nucleic Acids*, Wiley, New York .
49. Lu, J., Cistola, D. P., and Li, E. (2003) Two homologous rat cellular retinol-binding proteins differ in local conformational flexibility, *J. Mol. Biol. 330*, 799−812.
50. Mandel, A. M., Akke, M., and Palmer, A. G., 3rd (1995) Backbone dynamics of Escherichia coli ribonuclease HI: correlations with structure and function in an active enzyme, *J. Mol. Biol. 246*, 144−63.
51. Yuan, Y., Simplaceanu, V., Lukin, J. A., and Ho, C. (2002) NMR investigation of the dynamics of tryptophan side-chains in hemoglobins, *J. Mol. Biol. 321*, 863−78.
52. Clore, G. M., Gronenborn, A. M., Szabo, A., and Tjandra, N. (1998) Determining the magnitude of the fully asymmetric diffusion tensor from heteronuclear relaxation data in the absence of structural information, *J. Am. Chem. Soc. 120*, 4889−90.
53. Riek, R., Fiaux, J., Bertelsen, E. B., Horwich, A. L., and Wüthrich, K. (2002) Solution NMR techniques for large molecular and supramolecular structures, *J. Am. Chem. Soc. 124*, 12144−53.
54. Millet, O., Loria, J. P., Kroenke, C. D., Pons, M., and Palmer, A. G., 3rd (2000) The static magnetic field dependence of chemical exchange linebroadening defines the NMR chemical shift time scale, *J. Am. Chem. Soc. 122*, 2867−77.
55. Cronet, P., Petersen, J. F., Folmer, R., Blomberg, N., Sjoblom, K., Karlsson, U., Lindstedt, E. L., and Bamberg, K. (2001) Structure of the PPARalpha and -gamma ligand binding domain in complex with AZ242; ligand selectivity and agonist activation in the PPAR family, *Structure 9*, 699−706.
56. Johnson, B. A., Wilson, E. M., Li, Y., Moller, D. E., Smith, R. G., and Zhou, G. (2000) Ligand-induced stabilization of PPARgamma monitored by NMR spectroscopy: implications for nuclear receptor activation, *J. Mol. Biol. 298*, 187−94.
57. Yan, X., Broderick, D., Leid, M. E., Schimerlik, M. I., and Deinzer, M. L. (2004) Dynamics and ligand-induced solvent accessibility changes in human retinoid X receptor homodimer determined by hydrogen deuterium exchange and mass spectrometry, *Biochemistry 43*, 909−17.
58. Vivat-Hannah, V., Bourguet, W., Gottardis, M., and Gronemeyer, H. (2003) Separation of retinoid X receptor homo- and heterodimerization functions, *Mol. Cell. Biol. 23*, 7678−88.
59. Kallenberger, B. C., Love, J. D., Chatterjee, V. K. K., and Schwabe, J. W. R. (2003) A dynamic mechanism of nuclear receptor activation and its perturbation in a human disease, *Nat. Struct. Biol. 10*, 136−40.

BI051474J